RESEARCH ARTICLE | MARCH 14 2025

Compact beam position monitor using a segmented toroidal coil

F. Abusaif ; F. Hinder ; A. Nass ; J. Pretz ; F. Rathmann ; H. Soltner ; D. Shergelashvili ; R. Suvarna ; F. Trinkel

Rev. Sci. Instrum. 96, 033302 (2025)
https://doi.org/10.1063/5.0240076

Review of Scientific Instruments ARTICLE pubs.aip.org/aip/rsi

Compact beam position monitor using a segmented toroidal coil

Cite as: Rev. Sci. Instrum. 96, 033302 (2025); doi: 10.1063/5.0240076
Submitted: 24 September 2024 • Accepted: 13 February 2025 •
Published Online: 14 March 2025

F. Abusaif,[1,2,3] F. Hinder,[1,2] A. Nass,[2] J. Pretz,[1,2,a)] F. Rathmann,[2,4] H. Soltner,[5] D. Shergelashvili,[6] R. Suvarna,[1,7] and F. Trinkel[1,2,8]

AFFILIATIONS

[1] Physics Institute III B, RWTH Aachen University, 52074 Aachen, Germany
[2] Institute for Nuclear Physics, Forschungszentrum Jülich, 52425 Jülich, Germany
[3] Institute for Beam Physics and Technology, Karlsruhe Institute of Technology, 76131 Karlsruhe, Germany
[4] Brookhaven National Laboratory, Upton, New York 11973, USA
[5] Institute of Technology and Engineering, Forschungszentrum Jülich, 52425 Jülich, Germany
[6] High Energy Physics Institute, Tbilisi State University, 0186 Tbilisi, Georgia
[7] GSI Helmholtz Centre for Heavy Ion Research, 64291 Darmstadt, Germany
[8] German Aerospace Center (DLR), Linder Höhe, 51147 Köln, Germany

[a)] **Author to whom correspondence should be addressed:** pretz@physik.rwth-aachen.de

ABSTRACT

An inductive compact beam position monitor based on a segmented toroidal coil surrounding the charged particle beam has been investigated. It makes use of the induced voltages in the windings instead of the induced charge imbalance on capacitor plates in the popular beam position monitors. We theoretically investigate the response of the coils to the bunched particle beam based on a lumped-element model and compare it to the measurements in the laboratory and in the storage ring COSY in terms of beam displacement. As to the frequency response of the coils, we find a resonant behavior, which may be exploited to further increase the sensitivity of the device. The resolution presently achieved is about 5 μm in a 1 s time interval for a beam current of 0.5 mA.

I. INTRODUCTION

Experiments searching for electric dipole moments (EDMs) of charged particles using storage rings are at the forefront of the incessant quest to find new physics beyond the Standard Model (SM). These investigations bear the potential to shed light on the origin of the hitherto unexplained large matter–antimatter asymmetry in the Universe.[1,2] The combined predictions of the SM of particle physics and of cosmology fall short of the experimentally observed asymmetry by about seven to eight orders of magnitude.[3]

The JEDI collaboration (Jülich Electric Dipole moment Investigations, see http://collaborations.fz-juelich.de/ikp/jedi) is currently leading the effort to scrutinize the technical feasibility of the storage ring approach to the determination of the EDMs of protons.[4] In the framework of systematic beam and spin dynamics studies, a dedicated experiment to determine the deuteron EDM[5–7] is presently being carried out at the storage ring COSY (Cooler Synchrotron COSY at Forschungszentrum Jülich, Germany[8,9]). Its basic parameters are given in Table I.

Given the extremely small anticipated values of the EDMs of the charged particles, down to 10^{-29} e cm, the control of systematic effects in the ring is of paramount importance, and high-precision monitoring of the positions of the beams in the ring constitutes one of the great challenges in these experiments. This entails precise control of the beam position along the lattice of the ring, thus a precise control of the beam orbit. In order to improve the knowledge about the absolute beam orbit in COSY, various alignment campaigns had been conducted, during which all magnetic elements in the machine were positioned to an accuracy of about 0.2 mm, or 0.2 mrad, respectively. In addition, absolute beam-offset

TABLE I. Parameters of the Rogowski coil and of COSY. The electrical parameters C, L, and R are calculated in Appendix B. Typical beam parameters for a momentum p are listed. e denotes the elementary charge.

Parameter	Value
Number of quadrants M	4
Toroid large radius	$R_t = 58.5$ mm
Toroid small radius	$a = 6.0$ mm
Ratio parameter	$b = a/R_t = 0.1026$
Wire diameter	$d_w = 450\ \mu$m
Windings per quadrant	$N_w = 132$
Angular coverage	$\Delta\theta = 64°$
Capacitance per quadrant (wiring)	$C \approx 20.7$ pF
Inductance per quadrant	$L \approx 41.4\ \mu$H
Ohmic resistance of quarter coil	$R \approx 0.61\ \Omega$
Input impedance	$R_{out} \approx 500\ k\Omega$
Resonance frequency (estimated)	$f_0 \approx 5.88$ MHz
Beam momentum	$p = 970$ MeV/c
Revolution frequency	$f_{rev} = 750\,197.3$ Hz
Lorentz factor	$\beta = 0.459$
Number of stored particles	$N = 10^9$
Corresponding beam current	$I = e\,N\,f_{rev} = 120.2\ \mu$A
Circumference	183.47 m
Typical bunch length	20 m

parameters for each of the installed beam position monitors (BPM) were obtained from a dedicated beam-based alignment effort, as described in Ref. 10.

The BPMs used at COSY[8] are capacitive measuring devices. The position of the beam is determined based on the induced charge imbalance on opposing capacitor plates. The typical insertion length of such a pair of BPMs along the beam direction, providing horizontal x and vertical y positions, amounts to about 500 mm. For beams comprising ~10^9 particles, capacitive BPMs provide a resolution of a few μm for a measurement time of 1 s and an accuracy of about 100 μm.

These capacitive BPMs, however, appear unattractive because their length limits the number of devices that can actually be installed in a machine. It is, therefore, imperative to develop alternative BPMs that require significantly less installation space. The inductive BPM presented in this work offers the same resolution compared to the capacitive ones installed in COSY using only 10% of insertion length. It was not possible to install conventional BPMs in front of and behind a one m long radio frequency Wien filter,[11] essential for the EDM experiments.

A general overview on BPMs is given in Ref. 12. References 13–15 describe conventional capacitive BPMs. The physics background of BPMs has been highlighted by Refs. 16 and 17. More specifically, inductive BPMs have been described, e.g., in Refs. 18–20. Reference 20 points out that inductive devices can be very short and are less prone to beam charge effects.[21] In our publication, we describe an approach based on the *induction* of voltages in opposing segments of a compact toroidal coil, which is passed through by the bunched beam, providing a position value based on the measured voltage imbalance. Previous studies of our group are discussed in proceedings[22] and in a PhD thesis.[23] Prior to our work, the so-called Rogowski coils for the determination of the beam current and position were discussed in Ref. 24. In this article, we will discuss the theoretical description and the resonant behavior in detail.

One advantage of induction coils for this particular application, apart from their mechanical simplicity, is that they offer a large sensor surface in a small volume due to the large number of windings. In addition, they can be operated in resonance to increase the induced voltage, and therefore, due to the induction principle, they benefit from the high revolution frequency of the bunched-beam signals in a ring accelerator. Furthermore, it should be noted that BPMs based on induction coils are sensitive to the time derivative of the beam current $\dot{I}$, whereas, the signal output of capacitive BPM depends among other things on the bunch length and contains contributions proportional to I and $\dot{I}$.[25] Unlike BPM systems based on SQUIDs,[26] they do not necessarily require low temperatures or vacuum conditions during testing and beam operation, which facilitates their development in the laboratory. Because of their short insertion length of about 50 mm, Rogowski-type BPMs appear ideally suited for a future dedicated EDM storage ring; see Chaps. 7 and 8 of Ref. 4.

This paper is organized as follows: in Sec. II, the basic principles of BPMs based on toroidal coils are discussed. In Sec. III, the technical realization of the BPM, the experimental test stand, and the calibration procedure are described. Section IV summarizes the results of the investigations carried out at the test stand. The results of the measurements obtained after installation in the COSY storage ring are described in Sec. V, followed by the conclusions and outlook in Sec. VI. Detailed derivations of the signal induced in a quarter coil are discussed in Appendix A, the resonant frequency of a quarter coil in Appendix B, and the effect of mirror currents in Appendix C.

II. TOROIDAL COILS AS BEAM POSITION MONITORS

A. General considerations

Coils wound on a toroidal coil core are also called *Rogowski coils*, named after Walter Rogowski.[27] Such devices are used as AC current transformers and as beam current monitors, taking advantage of the fact that due to Ampère's law, the induced voltage in the coil is *independent* of the position of the current-carrying wire passing through it.[28–32] Rogowski coils are ideally suited for the application as BPMs because the magnetic flux lines of a current-carrying straight wire form concentric circles around the wire and penetrate the cross-sectional area of the windings of the Rogowski coil at right angles, resulting in an optimal induced potential difference between the ends of the coil. We used coils wound around a non-magnetic core. Note that using a magnetic core, the resonance frequency would be too low for our application and the coupling between the quarter coils would be higher.

B. Position response of a differential coil setup

The magnetic difference signal of two identical induction coil sensors is a measure of the position of the beam between them, as

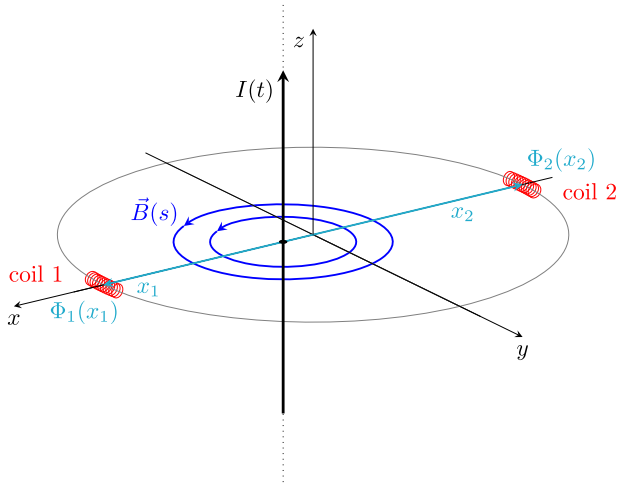

FIG. 1. Beam position response of two identical induction coils (1 and 2). The z axis points along the direction of the beam current $I(t)$. $\vec{B}(s)$ is the magnetic field created at a distance s from this beam current. The change of the induced magnetic flux Φ_1 and Φ_2, probed by the two coils, is sensitive to the displacement of the beam from the center $\Delta x = (x_2 - x_1)/2$.

derived in this section. The magnetic flux density generated by the beam current $I(t)$ can be written as

$$\vec{B}(t) = \frac{\mu_0 I(t)}{2\pi\, s}\vec{e}_t, \tag{1}$$

where $\vec{e}_t$ is a unit vector along the circumference, μ_0 is the vacuum magnetic permeability, and s is the radial distance from the beam center. As shown in Fig. 1, the beam is perpendicular to the plane defined by the two coils.

The time derivative of the induced flux in two identical short induction coils, 1 and 2, located on a circle of diameter d is given by

$$\dot{\Phi}_{1,2} = -\frac{U_{1,2}}{N_w} = \dot{B}_{1,2}\cdot S = \frac{\mu_0 \dot{I}}{2\pi}\frac{S}{x_{1,2}}, \tag{2}$$

where S denotes the cross-sectional area of the coils and N_w is the number of windings. The ratio of induced voltage difference to voltage sum in the two coils is, therefore, given by

$$\frac{\Delta U}{\Sigma U} = \frac{U_1 - U_2}{U_1 + U_2} = \frac{x_2 - x_1}{x_2 + x_1} = \frac{2\Delta x}{d}. \tag{3}$$

The above-mentioned considerations also apply to rotationally symmetric charge distributions of the beam, as discussed in more detail in Sec. II C.

The above-mentioned derivation illustrates that a suitably segmented toroidal coil may serve as a BPM. Due to symmetry considerations, the induced voltage difference is an odd function of the beam displacement, thus yielding a linear relationship for small displacements, as illustrated in Eq. (3). A toroidal coil segmented into four elements, as indicated in Fig. 2, allows one to simultaneously determine the beam position along two orthogonal coordinate axes. This specific segmentation will be discussed further in this publication.

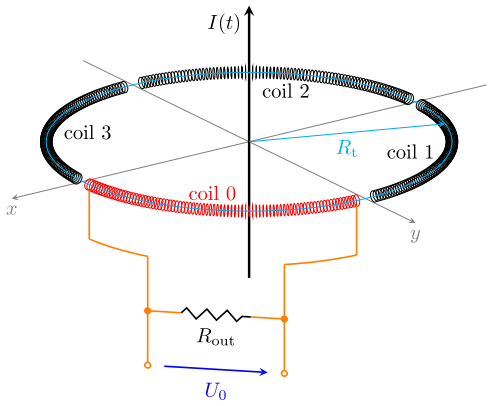

FIG. 2. Toroidal coil of radius R_t, segmented into four quadrants ($M = 0, 1, 2, 3$). The (beam) current $I(t)$ passes through the coil along the z axis. The induced voltage U_0 in one quarter is measured by using a device with an input impedance of R_{out} (also see the equivalent circuit diagram in Fig. 3).

C. Evaluation of the flux in a quarter coil

For the calculation of the flux encircled by the windings on the torus, we start from the vector potential $\vec{A}$, which is linked to the beam current density $\vec{j}$ via Poisson's equation. Using cylindrical coordinates, ρ, φ, and z, one finds

$$\Delta\vec{A}(\rho,\varphi,z) = -\mu_0 \cdot \vec{j}(\rho,\varphi,z), \tag{4}$$

when displacement currents are neglected. If the beam current has only a component in the z direction, as shown in Fig. 1, the same holds for the vector potential $\vec{A}$, and we can regard the problem as two-dimensional. Furthermore, here we consider beams with rotationally symmetric current distributions that are much smaller than the coil diameter $d = 2R_t$, so that no beam particles intercept the Rogowski coil. Such a current distribution generates a field in its outside region that bears no information about the radial current distribution and is, therefore, equivalent to a pencil beam.[33] In this case, the remaining component of the vector potential A_z is a harmonic function outside the beam, i.e., $\Delta A_z = 0$, which is given by the logarithm of the distance to the beam. Thus, in cylindrical coordinates, we arrive at the ansatz,

$$A_z(\rho,\varphi) = -\frac{\mu_0 I}{2\pi}\ln\left(\sqrt{(\rho\,\cos\,\varphi - x)^2 + (\rho\,\sin\,\varphi - y)^2}\right). \tag{5}$$

In order to find the induced flux, an integration of A_z along the wire path $\vec{\ell}$ has to be performed.

The calculation of the induced magnetic fluxes Φ_M in the four quadrants $M = 0, 1, 2, 3$, discussed in Appendix A, yields a power expansion in terms of the beam displacements x and y. The corresponding induced voltages for any Fourier component of the periodic beam current in the storage ring are given by differentiation, which is conveniently carried out in the frequency domain by using $\omega = 2\pi f$.

Making use of Eq. (B2), we consider the amplitudes,

$$U_M = F(\omega)U_M^{\text{ind}} = -F(\omega)\dot{\Phi}_M = -F(\omega)\omega\Phi_M, \tag{6}$$

where the frequency response $F(\omega)$ is included because the quarter coil is operated in a resonance regime. Using Eq. (A18), one obtains for the induced voltage in a quadrant M,

$$\begin{aligned} U_M(x,y,\omega) &= F(\omega)U_M^{\text{ind}}(x,y) \\ &= \hat{U}(\omega)\left(D_0(b) + \sum_{m=1}^{\infty} D_m(b)\cdot E_{m,M}(x,y)\right), \end{aligned} \tag{7}$$

where

$$\hat{U}(\omega) = \mu_0 a N_{\text{w}}\ \omega F(\omega) I,$$

where N_{w} is the number of windings and b denotes the ratio of the small radius a of the coil to the large radius R_{t} of the toroid (see Table I and Fig. 17). The geometric functions $D_m(b)$ are defined in Eq. (A17), listed in Table III, and analytical expressions for the $E_{m,M}(x,y)$ are given in Table IV in Appendix A. For vanishing beam displacements $E_{m,M}(0,0) = 0$, the remaining $D_0(b)$ describes the common voltage induced in each of the quadrants. The frequency response $F(\omega)$ is discussed in Sec. II D and Appendix B. The higher-order terms in the sum describe the non-linearity of the device when larger beam displacements are encountered.[34]

The symmetries that apply to the induced flux in the different quadrants are passed on to the induced voltages of the quadrants [see Eq. (A20)]. Given the induced voltage $U_0(x,y)$ from Eq. (7), one can write for the induced voltages in the other quadrants,

$$\begin{aligned} U_1(x,y) &= U_0(-x,y), \\ U_2(x,y) &= U_0(-x,-y), \\ U_3(x,y) &= U_0(x,-y). \end{aligned} \tag{8}$$

Therefore, assuming identical segments, the sum over the voltages of all quadrants is independent of the beam displacements,

$$U^{\Sigma} = \sum_{M=0}^{3} U_M = 4\ \hat{U}D_0(b). \tag{9}$$

This property makes it possible to monitor the current of a bunched beam with an *unsegmented* Rogowski coil.

Small beam displacements can be adequately described by the linear term in Eq. (7), corresponding to $m = 1$ in the sum. Thus, to lowest order,

$$\begin{aligned} U_0 &\approx \hat{U}(\omega)\cdot[D_0(b) + D_1(b)\cdot E_{1,0}(x,y)] \\ &= \hat{U}(\omega)\cdot\left[\frac{1-\sqrt{1-b^2}}{b}\ \frac{2\Delta\theta}{\pi} + \frac{2}{b\pi}\left(\frac{1}{\sqrt{1-b^2}} - 1\right)\right. \\ &\quad \left.\cdot\frac{x+y}{R_{\text{t}}}\ (\cos(\theta) - \sin(\theta))\right], \end{aligned} \tag{10}$$

where the angles θ and $\Delta\theta$ are defined in Fig. 5. The linear term in the displacements x, y is the basis for the operation of opposed quadrants or halves as BPMs, if the corresponding signals are subtracted.

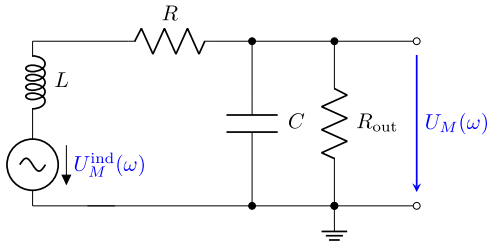

FIG. 3. Equivalent circuit diagram for one toroidal coil quadrant with inductance L, as shown in Fig. 2. A voltage $U_M^{\text{ind}}(\omega)$ is induced due to the inductive coupling of the beam inside the coil. The resistance of the quadrant coil is R, and its capacitance C is mostly due to the connecting wires. R_{out} represents the input impedance of the preamplifier.

D. Frequency response

Before we discuss, in Sec. III, the specifics of the design of a BPM based on a segmented toroidal Rogowski coil, the frequency response of such a system shall briefly be addressed. The basic setup of a toroidal coil that is split into four individual quadrants is shown in Fig. 2. The equivalent circuit diagram for a single quadrant coil coupled to the beam circuit is depicted in Fig. 3.

The voltage U_M due to the induction by the orbiting bunched beam is modified by the resistance R of the coil wire, by the inductance L of the coil, and by the capacitance C. The latter is largely due to the connecting wires, as shown Appendix B. The windings of the coil can be regarded as capacitors in a series. The total capacitance is then the capacity of two windings divided by the number of turns, which results in a value of less than 1 pF. This is negligible compared to the capacitance between the connecting wires.[35] The equivalent wavelength corresponding to the revolution frequency of the beam is large compared to the size of the BPM; thus, one can treat these components as lumped elements, as shown in the equivalent circuit diagram in Fig. 3. The resistor R_{out} describes the input impedance of the measuring device.

These lumped elements, C, L, R, and R_{out} constitute a resonant circuit. Its frequency response $F(\omega)$ with the values given in Table I is calculated in Appendix B. This yields for a quarter coil, an estimated resonant frequency of $f_0 \approx 5.88$ MHz.

One would ideally operate the coil quarters at resonance to take advantage of the amplified voltage in order to improve the signal-to-noise ratio. The disadvantage is that small shifts in the resonance frequency due to external conditions (e.g., temperature drifts) may lead to large changes in the amplifying factors of the four coils. Due to manufacturing tolerances, the four resonance curves are not absolutely identical, which may, therefore, lead to changes in the position measurement. For this reason, the decision was made to operate the segmented coils off-resonance.

The Rogowski coils were designed for operation at a frequency of 3 MHz, i.e., with four bunches orbiting in the storage ring at a revolution frequency of 750 kHz. The final experiment was carried out in a single-bunch mode, thus calibrations and measurements were performed at 750 kHz, i.e., far away from the resonant frequency. The resonant frequency of the coils was adjusted to a common value by placing appropriate capacitors parallel to the coils. This was done in order to guarantee that small changes in the resonance curves affect all the coils in the same way.

III. EXPERIMENTAL REALIZATION

A. Physical parameters of the Rogowski BPM

The Rogowski BPM described here consists of four equal coil segments, as illustrated in Fig. 4, ⓐ. Each coil is connected to a preamplifier[36] ⓕ, which, in total, delivers four voltage signals that are combined in software to yield the differential signals of two sets of opposing half coils, which serve to simultaneously determine the beam displacement in x and y directions.

PEEK plastic (polyether ether ketone, material properties are given in https://pubchem.ncbi.nlm.nih.gov/compound/19864017) was chosen as the supporting torus for the coils because of its low cost, good machineability, and low outgassing rates in vacuum. The earlier used Vespel® material (for material properties, see https://www.dupont.com/products/vespel.html) proved worse in terms of price and showed higher outgassing rates, mostly due to absorbed water. The coil torus features a groove along its outer circumference and small radial bore holes for the returning quarter coil wires and their fixation, respectively.

The inner and outer diameters of the toroid onto which the Rogowski coils are wound amount to 105 and 129 mm, respectively, sufficiently large to avoid any obstruction of the beam inside the circular beam tube diameter of 150 mm in the COSY straight sections. The Kapton-insulated copper wire for the sensor coils has a diameter of 450 μm. The number of windings (N_w = 132) determines the inductance of the quarter sensor coil and thus its resonant frequency, as discussed in Sec. II D. The calculated ohmic resistance of the coil is $R \approx 0.61\ \Omega$. The inductance can be estimated from the textbook formula of a straight coil with the same length, which yields a value of $L \approx 41.4\ \mu$H.

To install the coil in the CF 160 flange, it is clamped between two PEEK rings held together by screws of the same material. Each coil features a twisted wire pair with a length of 10 cm, connected to a 16 cm long coaxial cable, terminated with an SMA connector at the end that connects to an SMA UHV feedthrough on a CF 16 flange. Figure 5 shows a photograph of the fully assembled BPM as it was used both on the test bench and in the storage ring.

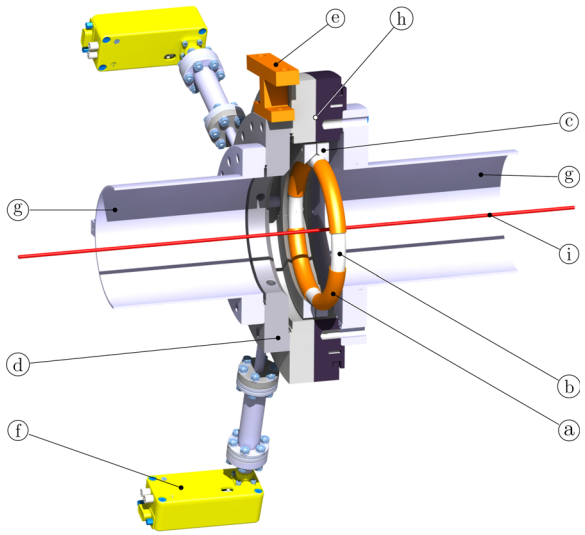

FIG. 4. Internal structure of the setup of the toroidal coil support in the test stand, depicted in Fig. 6: ⓐ Toroidal quarter coils on torus, ⓑ coil supporting torus (PEEK), ⓒ coil supporting rings (PEEK), ⓓ DN 100/150 CF coil supporting flange ⓔ fiducial mark, ⓕ coaxial feedthrough with a preamplifier, ⓖ DN 150 CF beam line vacuum tubes, ⓗ rotary flange, and ⓘ current carrying wire.

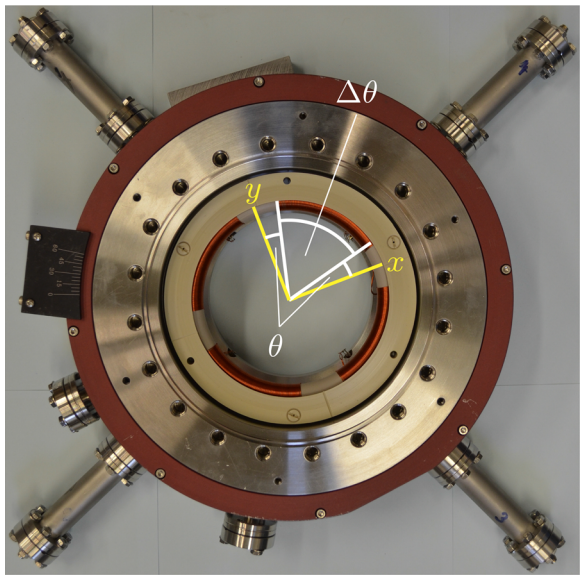

FIG. 5. Photograph of the Rogowki BPM installed in the rotary flange, as shown in Fig. 4. The coil covers an angle $\Delta\theta$. Note that $\Delta\theta + 2\theta = 90°$.

B. Test stand for the Rogowski BPM

The laboratory test stand, shown in Fig. 6, has been developed for the purpose of conditioning and calibrating Rogowski BPMs prior to the installation at COSY. The BPM is fixed on top of a stepper motor-driven xy table ⓚ, ⓘ in order to displace it laterally with respect to a current carrying tin-coated (corrosion-free) copper wire ⓘ, which mimics the particle beam in COSY. A sinusoidal current from a signal generator (Keysight 33522B Waveform Generator, Keysight Technologies, www.keysight.com) of about 100 μA in amplitude represents the dominant Fourier component of the COSY beam current at the revolution frequency of 750 kHz. The wire with a length of about 1 m is fixed on one side in a xy table ⓜ for angular adjustment, and on the other side, it is guided by a roll and pulled by a weight in a water bath ⓝ to ensure a constant tension on the wire without vibrations. The current is fed into the wire close to the xy table. At the other end ⓘ of the test stand, the current passes a 50 Ω resistor before returning to the RF-generator.

Tubes ⓖ on both sides of the flange are added to mimic the electrical surroundings of the BPM in COSY. The stepper motors ⓚ ⓘ (LIMES 150-100-MiSM-IMS produced by OWIS GmbH, www.owis.eu) move the coil in the xy plane during a calibration measurement. They have a maximum travel range of 100 mm, a load capacity of 60 kg, and a positioning error of <10 µm. The repeatability of a specific position is better than 500 nm; the resolution of 50 nm is ensured by an encoder for each axis.

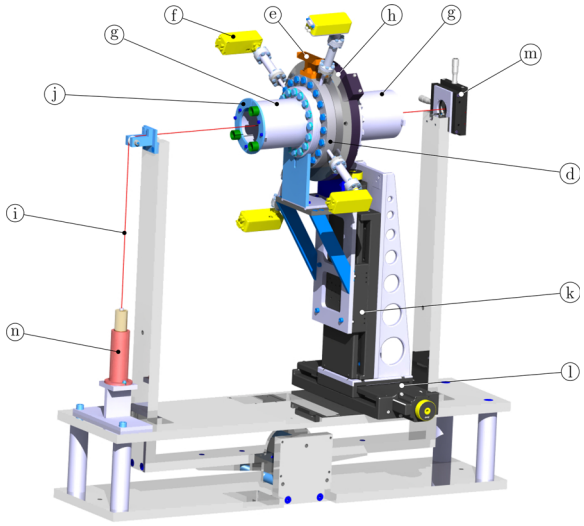

FIG. 6. Experimental setup to test and commission the Rogowski-type BPMs. The internal structure of the BPM is shown in Fig. 4. ⓓ DN 100/150 CF coil support flange, ⓔ fiducial mark, ⓕ coaxial feedthrough with preamplifier, ⓖ DN 150 CF beam line vacuum tubes, ⓗ rotary flange of the rf Wien filter, ⓘ current carrying wire, ⓙ tool with knife edges and fiducial marks (see Fig. 8), ⓚ vertical (y) stepper-motor drive, ⓛ horizontal (x) stepper-motor drive, ⓜ manual xy table for angular adjustment of the current-carrying wire, and ⓝ weight in water bath to stretch the wire and to damp its oscillations.

The analog signals from the coils are fed into custom-made preamplifiers[37] ⓕ with gain factors of about 18, measured at 750 kHz. The amplified signals are analyzed by lock-in amplifiers (Zurich Instruments HF2LI Lock-in Amplifier 50 MHz, 210 MSa/s www.zhinst.com) using the TTL signals from a second signal generator of the same type as the reference (Fig. 7). This was necessary to avoid crosstalk between the original signal and the reference signal when using two channels of the same device. Both generators were coupled to each other to assure that the generated frequencies were identical.

The analog-to-digital converters feature a resolution of 14 bit. A measurement bandwidth of 6.81 Hz with a fourth-order low-pass filter is typically used for signal conditioning. This entails a time constant of about 10 ms. The demodulator needs a 10 times larger time to reach 99% of the output level, which means that we are dealing with a minimum integration time of about 100 ms.

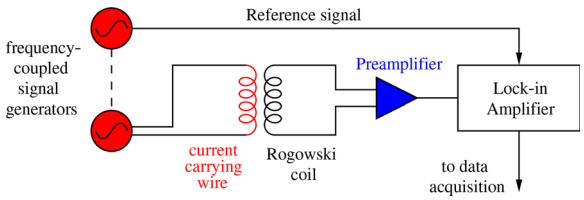

FIG. 7. Electric circuit diagram for the measurements with the experimental test setup, as shown in Fig. 6.

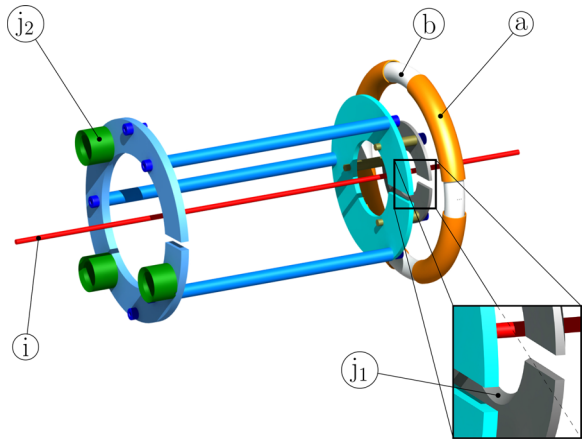

FIG. 8. Knife edge tool with knife edges ⓙ1 and fiducial marks ⓙ2, quarter coils ⓐ wound on the torus ⓑ. The current carrying wire is denoted by ⓘ.

C. Calibration of the Rogowski BPM

For relative calibration, the device is moved relative to the current carrying wire using the stepper motors ⓚ ⓘ, while the responses of the quarter coils are processed by the readout electronics. An array map is recorded covering the central part of the space inside the device (see Sec. IV C).

The absolute calibration was performed by using an insertion tool, as shown in Fig. 8. This insertion tool was manufactured to determine the exact position of the wire during the calibration measurements. It consists of a structure which positions a knife edge ⓙ1 in the plane of the Rogowski torus ⓑ and fiducial marks ⓙ2 to be used for a laser tracking system. The exact geometry was surveyed by using a measuring machine (ZEISS UPMC850, Carl Zeiss QEC GmbH www.zeiss.de) to an accuracy of <1 μm. This insertion can be installed at any time, making use of the slits in the disks without changing the position of the current wire. The wire ⓘ is put at an electrical potential and a programmed routine moves the Rogowski BPM with the insertion until the wire touches the knife edge. Using the known geometry of the insertion, the readings of the xy tables and a laser tracker (OMNITRAC 2, Automated Precision Inc. www.apimetrology.com), the absolute position of the measured calibration maps can be referenced to the fiducial mark ⓔ located on top of the Rogowski BPM (see Fig. 6) with an accuracy of <40 μm. After installation of the BPM in COSY, the position of the fiducial mark is determined within the COSY lattice using a laser tracker. Thus, the absolute position of the particle beam within the COSY lattice can be determined with an accuracy defined by the accuracy of the measurement of the laser tracker, which is in the range of 50–100 μm.

D. Vacuum compatibility

In addition to the required accuracy of the position measurement, the compliance with the vacuum standards of the accelerator is crucial. All the components of the Rogowski coil were cleaned and baked before assembly. In order to test the vacuum compatibility

before installation in the accelerator, a vacuum test stand was set up, which consists of a bakable chamber that is pumped by a 250 l/s turbo-molecular pump (comparable with the pumping speed at the installation point in COSY). A quadrupole mass analyzer was used to determine the composition of the rest gas in the chamber.

The use of PEEK as the material for the coil body and the Kapton-coated wire for the coils yielded small outgassing rates. The pressures reached after baking at 120 °C for a week were $<5 \times 10^{-9}$ mbar. The mass spectrum before baking showed a dominant water peak. After baking, the water is removed from the structure and the wire. To minimize water accumulation on the BPM during installation in the ring, the time it was exposed to air was minimized. The reason for this was that both the Kapton-insulated wire and the PEEK plastic adsorb water in air.

Attention was paid to the temperature during the baking process, as this takes place after the calibration of the coil (which was carried out in air, see Sec. III C and Fig. 6). To ensure that baking did not alter the calibration values, several test calibrations were carried out before and after baking, which showed that there was no difference in the calibration values within the previously mentioned accuracy.

IV. INVESTIGATIONS USING THE TEST STAND

A. Impedance measurement of a quarter coil

In order to characterize a single quarter coil following the equivalent lumped circuit of Fig. 3, an impedance measurement was performed using a vector network analyzer (Siglent SVA 1032X, SIGLENT Technologies www.siglenteu.com). The influence of the connection cable outside the vacuum vessel was taken into account in the calibration so that the results, shown in Fig. 9, represent the coil including the connection wires up to the vacuum flange (see Fig. 4). The preamplifier was not used for this measurement.

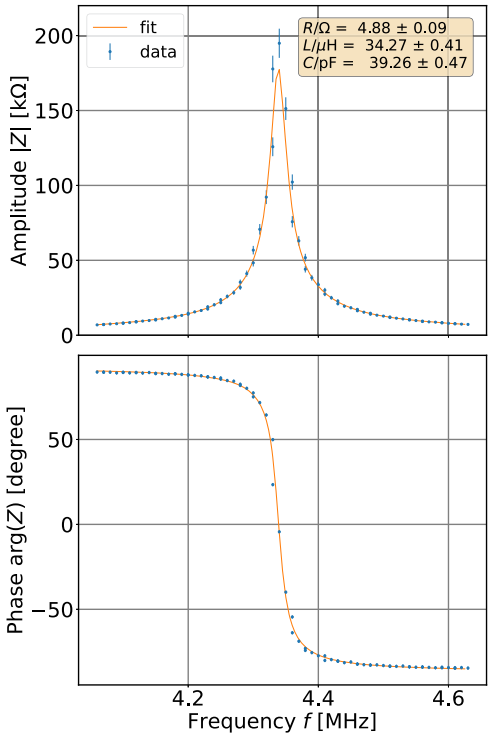

FIG. 9. Combined fit to the amplitude and phase data from the network analyzer according to Eq. (11).

The impedance of the coil can be expressed by

$$Z(\omega) = \left(i\omega C + \frac{1}{R + i\omega L}\right)^{-1}, \tag{11}$$

where R, L, and C are the respective properties of the circuit, as shown in Fig. 3. The amplitude and phase of Eq. (11) were used in a combined fit to determine these properties (Fig. 9). To improve the fit, an additional offset of the phase was introduced as a parameter. The value amounts to $-2.9(1)$ degrees. For the amplitude $|Z|$, a relative error of 5% was assumed, and for the phase $\arg(Z)$, the assumed error is 1°. These errors were estimated from the RMS of several measurements at the same frequency. The overall χ^2 value is 540. The amplitude contributes with 85 and the phase plot with 455 to the χ^2 value. The number of degrees of freedom is 160 (data points) − 4 (parameters) = 156. A possible correlation between amplitude and phase data is not taken into account. The resulting properties are the ohmic resistance $R = 4.88(9)\ \Omega$, the inductance $L = 34.27(41)\ \mu$H, and the capacitance $C = 39.26(47)$ pF. The DC resistance of the coil was measured to be about 1 Ω. For the copper wire used in the experiment, we expected an increase in the ohmic resistance by a factor of four due to the skin effect, roughly in agreement with the fit parameters.

B. Measurement of the resonant behavior of a quarter coil

The resonant behavior of a quarter coil was measured on the test setup, as shown in Fig. 6, using a sinusoidal signal of variable frequency on a wire to mimic the beam current. The induced currents in the four coils were amplified, and their output voltage signals measured using the lock-in amplifiers, as described in Sec. III B. The result of a frequency sweep for a single quarter coil is shown in Fig. 10. The amplitude and phase are given by Eqs. (B2) and (B3).

To better fit the data, the heuristic parameters s_p, s_R, and Φ_0 were introduced, yielding

$$\tilde{U}_M(\omega) = (1 + s_U\omega)F(R_{\text{out}}, L, C, R', I, \omega)U_M^{\text{ind}}, \tag{12}$$

where

$$R' = R(1 + s_R(\omega - \omega_0)), \tag{13}$$

$$\phi'(\omega) = (1 + s_p\omega)\phi - \phi_0. \tag{14}$$

These additional parameters account for other resonances present in the system and for the skin/proximity effect.[38] Due to the strong correlation between C and L, the value of L was fixed to the value from the impedance fit. The input impedance of the preamplifiers was assumed as $R_{\text{out}} = 500\ \text{k}\Omega$. The results of the fit are summarized in Table II.

For $\tilde{U}_M$, a relative error of 1% was assumed, and for the phase, the assumed error is 1°. The χ^2 value is 52.4 and has a contribution

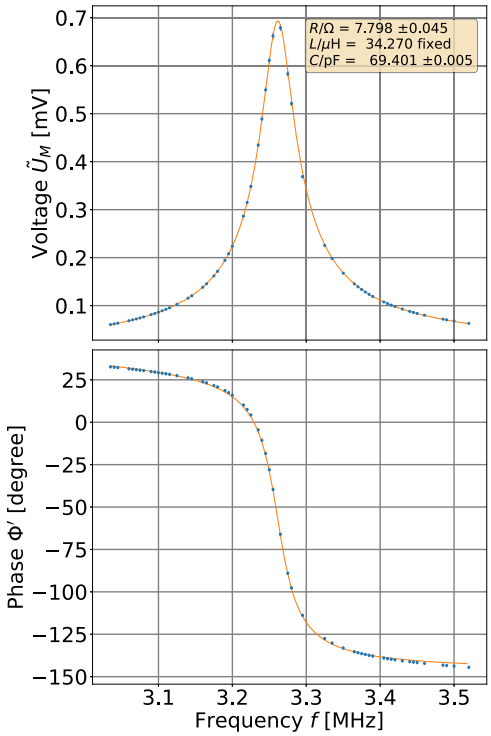

FIG. 10. Combined fit to the amplitude and phase data of one quarter coil excited by the current-carrying wire on the test stand.

TABLE II. Parameters of the fit to the resonance data shown in Fig. 10.

Fit parameter	Value
R	7.798(45) Ω
L Fixed	34.27 μH
C	69.401(5) pF
R_{out} fixed	500 kΩ
U_M^{ind}	9.12(1) mV
s_U	$8.0(2) \times 10^{-8}$ s^{-1}
s_p	$-2.4(2) \times 10^{-8}$ s^{-1}
s_R	$8.3(4) \times 10^{-7}$ s^{-1}
ϕ_0	152.5(2)°

of 16.3 from the amplitude and 36.1 from the phase. The number of degrees of freedom is $2 \cdot 58(\text{bins}) - 7(\text{parameters}) = 109$.

The equivalent circuit of Fig. 3, together with the additional parameters discussed above, describes the data very well. The increased resistance R and capacitance C compared to the impedance measurement are due to the preamplifier.

It was noticed that due to manufacturing tolerances, the resonance curves slightly differed for the four coils. This resulted in a strong frequency dependence of the calibration. As already mentioned before, this effect was reduced by additional variable capacitors, which shifted the resonance frequencies of all coils to a common value.

C. Calibration measurement of the BPM

The calibration measurement was carried out as described in Sec. III C. A map of 21 × 21 = 441 points is measured in the xy plane in the range ±10 mm. The four voltages, U_M, of Eqs. (7) and (8) were recorded and processed as follows:

$$U^{\Delta x} = U_0 - U_1 - U_2 + U_3,$$
$$U^{\Delta y} = U_0 + U_1 - U_2 - U_3. \tag{15}$$

Using U^{Σ} from Eq. (9), the ratios $U^{\Delta x}/U^{\Sigma}$ and $U^{\Delta y}/U^{\Sigma}$ are shown as a function of x and y, respectively, in Fig. 11. For better visibility of the data, the graphs are shifted proportionally by the respective y and x values. The first-order linear behavior clearly dominates. To get a good description of the data by the theory, additional parameters were introduced: the fit includes terms up to 4th order in m (see Appendix A). Despite the clamping mechanism of the torus, a perfect alignment angle could not be guaranteed; therefore, an angle α was added by which the xy coordinate system of the coils was rotated around the z axis. The coils are not exactly equal, therefore, small relative scaling coefficients $(1 + C_{sc})$ for the

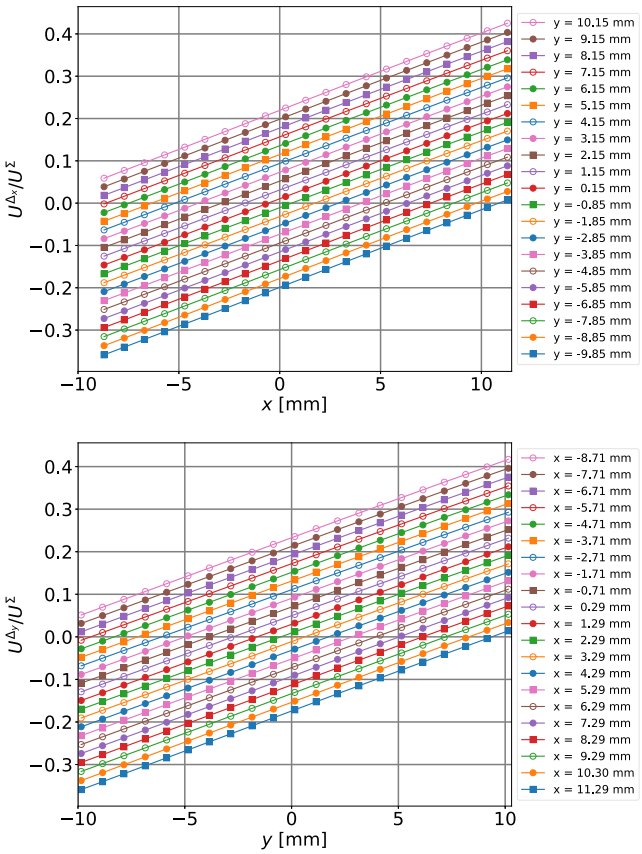

FIG. 11. Calibration map with the measured $U^{\Delta x}/U^{\Sigma}$ and $U^{\Delta y}/U^{\Sigma}$ values depending on the respective x and y positions set with the stepping drives of the xy table. For better visibility, the graphs are shifted by the respective y and x values.

voltages for three of the coils with respect to the fourth were introduced. From the RMS of repeated measurements, the error on $U^{\Delta_{x,y}}/U^{\Sigma}$ was estimated to be $2 \cdot 10^{-4}$. With this error assumption, a χ^2-minimization resulted in χ^2 values of 19.5 and 7.5 for the ratios U^{Δ_x}/U^{Σ} and U^{Δ_y}/U^{Σ}, respectively, for 441(measurement points) − 20(parameters) = 421 degrees of freedom (ndf). The low χ^2/ndf indicates that the errors on $U^{\Delta_{x,y}}/U^{\Sigma}$ were probably overestimated.

From the fitted parameters to model $U^{\Delta_{x,y}}/U^{\Sigma}$, one can now reconstruct x and y and compare these values to the selected x and y values. This is shown in Fig. 12. The residuals (reconstructed - selected) are of the order of few μm.

The linear coefficient c_1 of the curves in Fig. 11 can be derived from Eqs. (8)–(10) as

$$\begin{aligned} c_1 &= \frac{D_1 E_1}{D_0} \frac{1}{x+y} \\ &= \frac{1}{R_t\sqrt{1-b^2}} \frac{\cos(\theta) - \sin(\theta)}{\Delta\theta} \\ &\approx 0.0115\,\mathrm{mm}^{-1}, \end{aligned} \tag{16}$$

but the fitted values $c_1^{\mathrm{fit}} \approx 0.018\,\mathrm{mm}^{-1}$, which could also be estimated directly from Fig. 11, are substantially higher. This originates from the surroundings of the coil. c_1 was calculated for an air coil in an environment free of conducting material. Since the Rogowski coils are installed inside the beam tube (Fig. 4), secondary induction due to mirror currents on the inner surface of the beam tube needs to be considered. This effect is included in the modified coefficient [see Appendix C, Eq. (C8)],

$$\begin{aligned} c_1' &= c_1\left(1 + \frac{b^2 R_r^2}{2u^2 b\pi D_1(b)}\right) \\ &\approx c_1\left(1 + \frac{R_t^2}{2u^2}\right) \approx 0.015\,\mathrm{mm}^{-1}, \end{aligned} \tag{17}$$

with the inner radius of the beam tube $u = 76.5$ mm. This estimate is based on the simple geometry of a straight beam tube and explains qualitatively the difference between the fitted value and the calculated value of an air coil in Eq. (16).

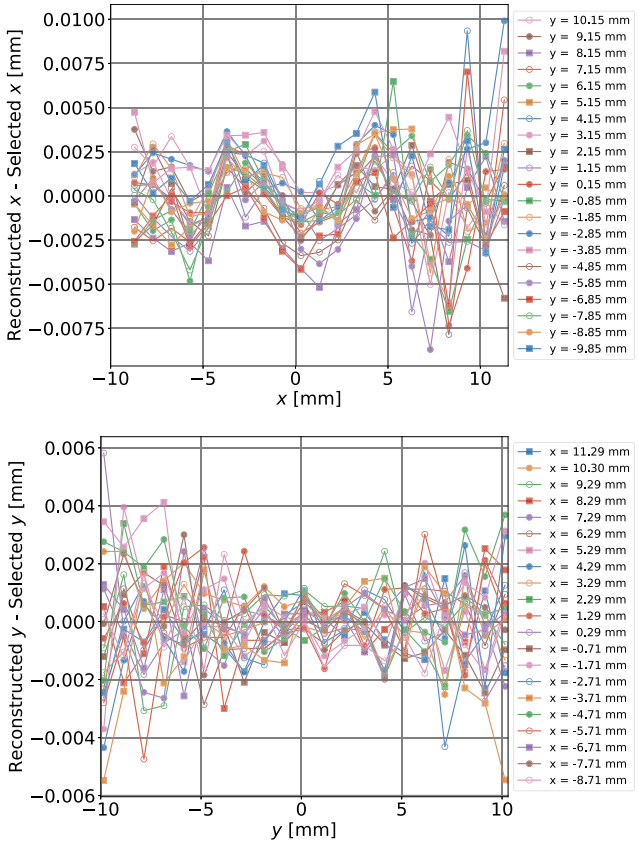

FIG. 12. Residuals: reconstructed x–selected x vs x (top) and reconstructed y–selected y vs y (bottom).

V. INSTALLATION AT COSY

After the calibration (Sec. IV C) and baking procedures (Sec. III D), the Rogowski BPM was installed at the storage ring COSY. It was noticed that an additional offset voltage present at zero beam current appeared. This offset compromised the position measurements, so that the position readings depended on the beam current, as shown in Figs. 13(a) and 14(a). The offset is due to stray fields of the COSY cavity, which is located at a distance of 9 m from the Rogowski coils. The eigen-frequency of the accelerating mode of this cavity defines the revolution frequency of the beam in COSY, which is also used as a reference frequency of the lock-in amplifier.

The offset voltage U_i^{off} was determined by extrapolating the measured voltages to zero beam current as can be shown for U_0 in Fig. 15. The interception of the straight line fit with the vertical axis yields the respective voltage offset corrections $U_0^{\mathrm{off}} = 775.4\,\mu\mathrm{V}$,

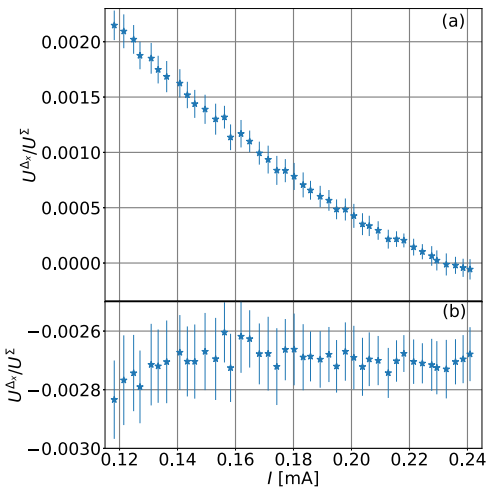

FIG. 13. U^{Δ_x}/U^{Σ} before (a) and after (b) offset correction. Without the correction, a drift depending on the beam current was observed in contrast to the measurements in the laboratory. The offset correction eliminates this dependence.

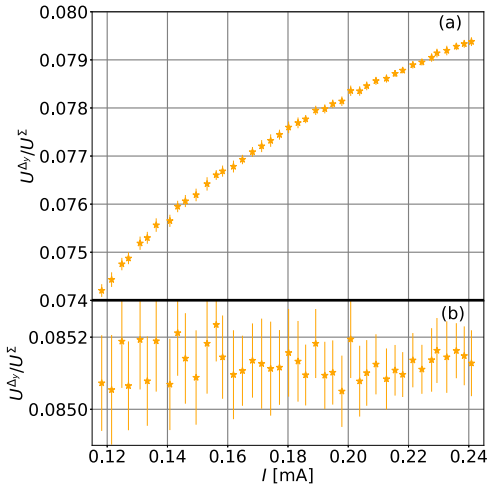

FIG. 14. U^{Δ_y}/U^{Σ} before (a) and after (b) offset correction. Without the correction, a drift depending on the beam current was observed in contrast to the measurements in the laboratory. The offset correction eliminates this dependence.

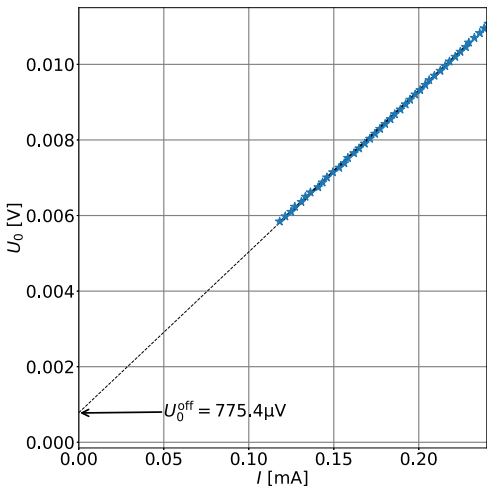

FIG. 15. Example of the induced voltage U_0 as a function of the COSY beam current I. The additional offset, due to stray fields, was determined by extrapolation to zero beam current.

$U_1^{\text{off}} = 749.5\,\mu\text{V}$, $U_2^{\text{off}} = 718.2\,\mu\text{V}$, and $U_3^{\text{off}} = 706.5\,\mu\text{V}$ for the four quarter coils. The subtraction of these offset values from the measured voltages resulted in beam current independent position values as expected from the calibration measurements in the laboratory [Figs. 13(b) and 14(b)]. Note that a change of 10^{-4} in the voltage ratio as shown in these figures corresponds to a change in the position of $10^{-4}/c_1^{\text{fit}} = 10^{-4}/0.018\text{mm}^{-1} \approx 5.5\,\mu\text{m}$. It can be seen that the error on a single measurement of a 1 s time interval is also of a similar amount, corresponding to a resolution of 5 μm.

The Rogowski BPM was used during several experimental beam times by the JEDI collaboration in order to determine the position of the COSY deuteron beam. Figure 16 show the measured

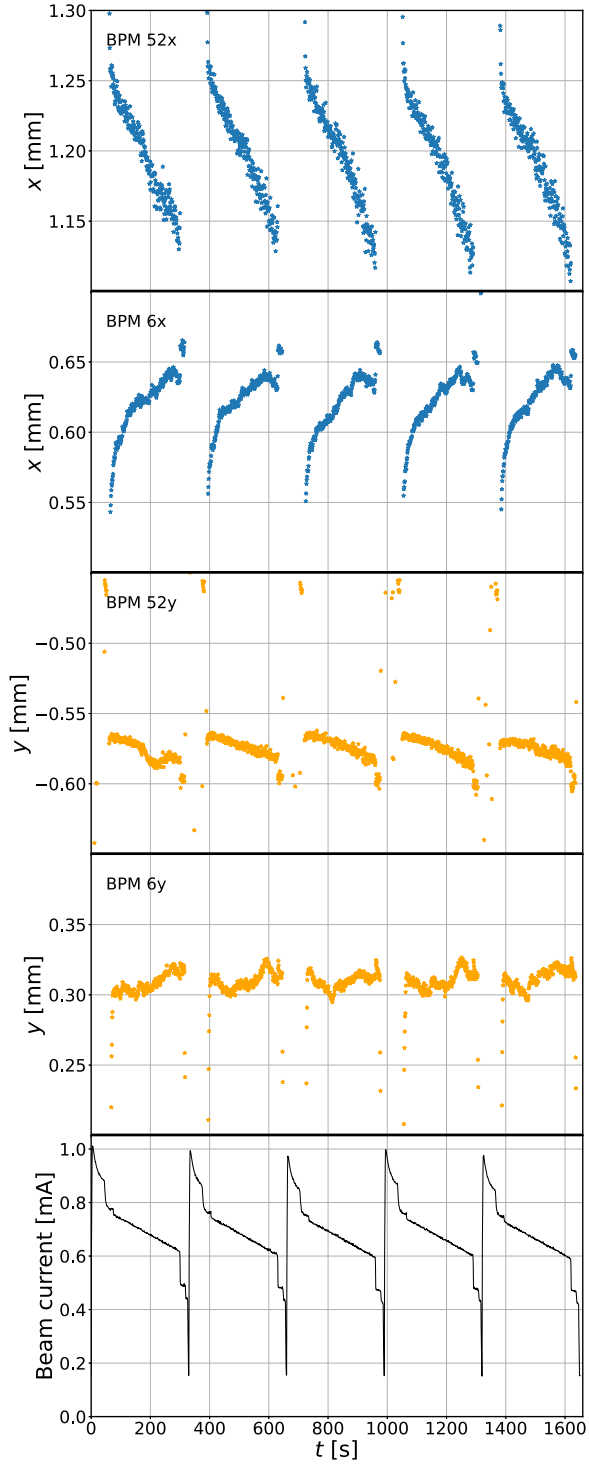

FIG. 16. Measured horizontal (52x) and vertical beam positions (52y) during five consecutive cycles in COSY. For comparison, the horizontal (vertical) position measurement of the next conventional COSY BPM (6x,6y) 4 m downstream in beam direction is shown. The lower plots show the beam current. Note that the drifts are in opposite directions, which are caused by quadrupole magnets in between the two devices.

beam position in horizontal and vertical directions for five consecutive cycles for the Rogowski coil (52x, 52y) and a conventional COSY BPM (6x, 6y).

VI. CONCLUSION AND OUTLOOK

We report on the technical development and the mathematical analysis of a beam position monitor based on a segmented toroidal coil, aka Rogowski coil. We have analytically derived the induced voltage in such a coil by a bunched particle beam, specifically with the search for electric dipole moments (EDMs) at storage rings in mind. Our analytical description comprises the application of a lumped-element model featuring the main electrical parameters of the coil. We were able to identify these values by means of impedance measurements and by the resonant excitation with a current carrying wire, which represents the particle beam in our dedicated test stand. While the values of capacitance and inductance can be motivated by naive estimates, the resistance required in the lumped element model is much larger than the dc-resistance of the coil due to skin effect and proximity effect. We also explained the enhancement of the induced voltages in the coil by mirror currents on the inside of the beam tube, which are induced by the particle beam. Thus, this publication provides a design guideline for researchers to apply such a BPM type to their beam line.

In experiments at the test stand and at COSY, we found that our coil-based BPM reaches a resolution of 5 μm in a 1 s time interval. The absolute accuracy is determined by the alignment accuracy of the device of about 50 μm. One advantage over classical capacitive BPMs is the short insertion length of these devices. In an energy-variable machine, the frequency-dependent amplification of the Rogowski BPMs limits its sensitivity because away from the resonance, the amplitude decreases. In the specific case of a fixed-energy EDM machine; however, this presents an advantage because, with an optimized design, the resonance enhances the signals.

While our development uses four toroidal coils, in principle, the device could be divided into more segments in order to study higher-order components of the transverse particle beam distribution. Note that the fourfold segmentation presented here already allows the study of the quadrupole moment of the beam. A pair of higher segmented Rogowski coils at a distance in the storage ring may offer the possibility to measure the phase space distribution of the particle beam.

The individual quarter coils have been measured separately in our investigations to yield the required differential voltage electronically after subtraction. A better read out scheme may be established by a direct galvanic connection between opposing quarters in order to inherently be sensitive to the differential signal without having to deal with the dominant contribution of the beam current represented by the term $D_0(b)$ in Eq. (10). This may also entail the development of a dedicated pre-amplifier for this purpose. In addition, the crosstalk between neighboring coils due to the mutually induced currents should be reduced in this way.

ACKNOWLEDGMENTS

This work has been performed in the framework of the JEDI collaboration and is financially supported by an ERC Advanced-Grant (srEDM No. 694390) of the European Union. We are very grateful to Jürgen Böker, Hans-Joachim Krause, Stefan Hintzen, Andrea Pesce, Thomas Sefzick, and Jamal Slim for their support.

AUTHOR DECLARATIONS

Conflict of Interest

The authors have no conflicts to disclose.

Author Contributions

F. Abusaif: Data curation (equal); Investigation (equal); Software (equal); Validation (equal). **F. Hinder**: Data curation (equal); Investigation (equal). **A. Nass**: Conceptualization (equal); Investigation (equal); Supervision (equal); Writing – original draft (equal). **J. Pretz**: Software (equal); Supervision (equal); Visualization (equal); Writing – original draft (equal). **F. Rathmann**: Conceptualization (equal); Formal analysis (equal); Investigation (equal); Supervision (equal); Writing – original draft (equal). **H. Soltner**: Conceptualization (equal); Formal analysis (equal); Writing – original draft (equal). **D. Shergelashvili**: Software (equal). **R. Suvarna**: Data curation (equal); Investigation (equal); Software (equal). **F. Trinkel**: Data curation (equal); Investigation (equal).

DATA AVAILABILITY

Raw data were recorded at the Cooler Synchrotron COSY and a test bench. Derived data supporting the findings of this study are available from the corresponding author on request.

APPENDIX A: DETAILED DERIVATIONS FOR AN ISOLATED COIL

Involving Stokes' theorem, the calculation of the magnetic flux due to the beam current enclosed by the winding surfaces S of a quarter coil with index $M = 0, 1, 2, 3$ can be expressed by the line integral of the vector potential over the boundary ∂S of the surface S,

$$\Phi = \iint_S \vec{B} \cdot \mathrm{d}\vec{S} = \oint_{\partial S} \vec{A} \cdot \mathrm{d}\vec{\ell}. \tag{A1}$$

The approach using the vector potential seems to be advantageous compared to the use of the B-field because in this case, we only have to deal with the single component A_z in order to obtain the enclosed magnetic flux. Furthermore, via Stokes' theorem, one integration less is required.

1. Derivation of magnetic flux induced in a quadrant coil

The surface of the torus with given values for R_t and a, as shown in Fig. 17, is parameterized in terms of the two angles φ and β, according to

$$\vec{\ell} = \begin{pmatrix} \ell_x(\beta,\varphi) \\ \ell_y(\beta,\varphi) \\ \ell_z(\beta) \end{pmatrix} = \begin{pmatrix} (R_t + a\,\cos\beta)\cdot\cos\varphi \\ (R_t + a\,\cos\beta)\cdot\sin\varphi \\ a\,\sin\beta \end{pmatrix}. \tag{A2}$$

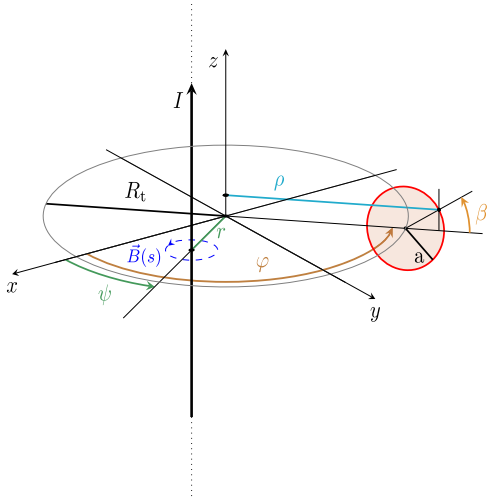

FIG. 17. Representation of the beam coordinates x and y, as given in cylindrical coordinates in Eq. (A7), and the location of one specific coil winding. The z axis points along the beam direction. The coil center coincides with the center of the coordinate system in the xy plane; the toroid is described by the two radii R_t and a. The two variables used for the integration are φ and β. The functional dependence of $\rho(\beta)$ is given in Eq. (A6).

The wire does not cover the surface of the torus entirely but follows a path given by a linear relation between the two angles φ and β,

$$\varphi(\beta) = u \cdot \beta. \tag{A3}$$

Due to the fact that the vector potential has only a component along the z direction, we only need the z component of the differential line element $\mathrm{d}\vec{\ell}$ along the coil winding, which is obtained by differentiation,

$$\mathrm{d}\ell_z(\beta) = a \cos\beta \, \mathrm{d}\beta. \tag{A4}$$

Furthermore, one has to consider that the coils do not cover the full torus. The angles θ and $\Delta\theta$ involved are indicated in Fig. 5.

The integral in Eq. (A1) can be further simplified, yielding for the flux induced in a quadrant M,

$$\begin{aligned}\Phi_M(x,y) &= \oint \vec{A}\cdot\mathrm{d}\vec{\ell} = \int A_z(\rho(\beta),\varphi(\beta))\,\mathrm{d}\ell_z \\ &= a\int_0^{2\pi\cdot N_w} A_z(\rho(\beta),\varphi(\beta))\cos\beta\,\mathrm{d}\beta \\ &= a\frac{2N_w}{\pi}\int_{M(\pi/2)+\theta}^{(M+1)(\pi/2)-\theta}\int_0^{2\pi} A_z(\rho(\beta),\varphi)\,\cos\beta\,\mathrm{d}\beta\,\mathrm{d}\varphi,\end{aligned} \tag{A5}$$

where

$$\rho(\beta) = R_t + a\cos\beta = R_t(1 + b\cos\beta), \tag{A6}$$

as shown in Fig. 17. In the last line of Eq. (A5), the sum over the N_w discrete angle values of φ is represented by an integral, which is an adequate description for a densely wound coil. In cylindrical coordinates, the vector potential $A_z(\rho,\varphi)$ has already been introduced in Eq. (5), in which the beam displacement from the center is parameterized in cylindrical coordinates,

$$x = r\cos\psi \quad \text{and} \quad y = r\sin\psi. \tag{A7}$$

Equation (5) can be written as

$$\begin{aligned}A_z(\rho,\varphi) &= -\frac{\mu_0 I}{2\pi}\ln\sqrt{\rho^2 - 2\rho r\cos(\varphi-\psi) + r^2} \\ &= -\frac{\mu_0 I}{2\pi}\left[\ln\rho - \sum_{m=1}^{\infty}\frac{1}{m}\left(\frac{r}{\rho}\right)^m\cos[m(\varphi-\psi)]\right],\end{aligned} \tag{A8}$$

where the latter part describes the decomposition into a Fourier series (see Eq. 3.152 in Ref. 39), for $r < \rho$. For a beam current monitor without segmentation of the toroidal coil, the integration over φ must be performed from 0 to 2π. Equation (A8) shows that all the cosine terms yield vanishing contributions in this case. Therefore, the information about the beam displacement encoded in ψ [see Eq. (A7)] vanishes as well. A full Rogowski coil without segmentation, therefore, constitutes a beam current monitor, its sensitivity being entirely described by the last logarithmic term in Eq. (A8), which depends only on the coil geometry.

For a toroidal coil segmented into four quadrants M, each covering $\Delta\theta \approx 64°$, however, the first integration over φ required in Eq. (A5) yields

$$\begin{aligned}A_z^{(1)}(\rho,M) &= \frac{2N_w}{\pi}\int_{M(\pi/2)+\theta}^{(M+1)(\pi/2)-\theta} A_z(\rho,\varphi)\,\mathrm{d}\varphi \\ &= -\frac{\mu_0 N_w I}{\pi^2}\left[\Delta\theta\ln(\rho) - \sum_{m=1}^{\infty}\frac{1}{m}\left(\frac{r}{\rho}\right)^m\right. \\ &\quad\cdot\left(\int_{M(\pi/2)+\theta}^{(M+1)(\pi/2)-\theta}\cos(m\varphi)\,\mathrm{d}\varphi\cdot\cos(m\psi) + \right. \\ &\quad\left.\left.\cdot\int_{M(\pi/2)+\theta}^{(M+1)(\pi/2)-\theta}\sin(m\varphi)\,\mathrm{d}\varphi\cdot\sin(m\psi)\right)\right] \\ &= -\frac{\mu_0 N_w I}{\pi^2}\left[\Delta\theta\ln\rho - \sum_{m=1}^{\infty}\frac{1}{m^2}\left(\frac{r}{\rho}\right)^m(c_{m,M}\cos(m\psi)\right. \\ &\quad\left.+ d_{m,M}\sin(m\psi)\right)\Big],\end{aligned} \tag{A9}$$

where the coefficients,

$$\begin{aligned}c_{m,M} &= \sin\left(m\pi\frac{M+1}{2} - \theta\right) - \sin\left(m\pi\frac{M}{2} + \theta\right), \\ d_{m,M} &= -\cos\left(m\pi\frac{M+1}{2} - \theta\right) + \cos\left(m\pi\frac{M}{2} + \theta\right)\end{aligned} \tag{A10}$$

are functions of the angle θ (see Table III). The dependence of the arguments of the trigonometric functions on m can be eliminated using a sum over the sine and cosine functions, related to

TABLE III. Analytical expressions for the terms $D_m(b)$ (Eq. (A17)) and the coefficients $c_{m,M}$ and $d_{m,M}$, defined in Eq. (A10), for the four quadrants M up to order $m = 6$ for a coil covering an angle $\Delta\theta$ starting at θ, i.e., $\pi/2 = \Delta\theta + 2\theta$. For small values of b, $D_m(b) \approx b/(m\pi)$.

M		0	1	2	3	0	1	2	3
m	$D_m(b)$	$c_{m,0}$	$c_{m,1}$	$c_{m,2}$	$c_{m,3}$	$d_{m,0}$	$d_{m,1}$	$d_{m,2}$	$d_{m,3}$
1	$\frac{2}{b\pi}\left(\frac{1}{\sqrt{1-b^2}}-1\right)$	$\cos\theta - \sin\theta$	$-c_{1,0}$	$-c_{1,0}$	$c_{1,0}$	$c_{1,0}$	$c_{1,0}$	$-c_{1,0}$	$-c_{1,0}$
2	$\frac{b}{2\pi\left(1-b^2\right)^{3/2}}$	0	0	0	0	$2\cos(2\theta)$	$-d_{2,0}$	$d_{2,0}$	$-d_{2,0}$
3	$\frac{b}{3\pi\left(1-b^2\right)^{5/2}}$	$-\cos(3\theta) - \sin(3\theta)$	$-c_{3,0}$	$-c_{3,0}$	$c_{3,0}$	$-c_{3,0}$	$-c_{3,0}$	$c_{3,0}$	$c_{3,0}$
4	$\frac{b\left(4+b^2\right)}{16\pi\left(1-b^2\right)^{7/2}}$	$-2\sin(4\theta)$	$c_{4,0}$	$c_{4,0}$	$c_{4,0}$	0	0	0	0
5	$\frac{b\left(4+3\,b^2\right)}{20\pi\left(1-b^2\right)^{9/2}}$	$\cos(5\theta) - \sin(5\theta)$	$-c_{5,0}$	$-c_{5,0}$	$c_{5,0}$	$c_{5,0}$	$c_{5,0}$	$-c_{5,0}$	$-c_{5,0}$
6	$\frac{b\left(8+12\,b^2+b^4\right)}{48\pi\left(1-b^2\right)^{11/2}}$	0	0	0	0	$2\cos(6\theta)$	$-d_{6,0}$	$d_{6,0}$	$-d_{6,0}$

the beam displacements x and y, via Eq. (A7). It follows with these trigonometric relations from Ref. 40 (1.331-1 and 1.331-3) that

$$A_z^{(1)}(\rho,M) = -\frac{\mu_0 N_w I}{\pi^2}\left[\Delta\theta\,\ln\rho - \sum_{m=1}^{\infty}\frac{1}{m^2}\left(\frac{r}{\rho}\right)^m\left(c_{m,M}\sum_{n=0}^{\lfloor\frac{m}{2}\rfloor}\binom{m}{2n}\right.\right.$$
$$\cdot(\cos\psi)^{m-2n}(\sin\psi)^{2n}(-1)^n + d_{m,M}\sum_{n=0}^{\lfloor\frac{m-1}{2}\rfloor}\binom{m}{2n+1}$$
$$\left.\left.\cdot(\cos\psi)^{m-(2n+1)}(\sin\psi)^{2n+1}(-1)^n\right)\right], \tag{A11}$$

where, e.g., $\lfloor m\rfloor \equiv \mathrm{floor}(m)$. In terms of the displacements, parameterized using Eq. (A7), one can then write

$$A_z^{(1)}(\rho,M) = -\frac{\mu_0 N_w I}{\pi^2}\left[\Delta\theta\,\ln\rho - \sum_{m=1}^{\infty}\frac{1}{m^2}\left(\frac{R_t}{\rho}\right)^m\left(c_{m,M}\sum_{n=0}^{\lfloor\frac{m}{2}\rfloor}\binom{m}{2n}\right.\right.$$
$$\cdot\left(\frac{x}{R_t}\right)^{m-2n}\left(\frac{y}{R_t}\right)^{2n}(-1)^n + d_{m,M}\sum_{n=0}^{\lfloor\frac{m-1}{2}\rfloor}\binom{m}{2n+1}$$
$$\left.\left.\cdot\left(\frac{x}{R_t}\right)^{m-(2n+1)}\left(\frac{y}{R_t}\right)^{2n+1}(-1)^n\right)\right]. \tag{A12}$$

The missing integration over β according to Eq. (A5), taking into account Eq. (A6), yields the magnetic flux,

$$\Phi_M(x,y) = a\int_0^{2\pi} A_z^{(1)}(R_t + a\cos\beta, M)\cos\beta\,\mathrm{d}\beta$$
$$= -\frac{\mu_0 N_w I a}{\pi^2}\left[\Delta\theta A^{(2)} - \sum_{m=1}^{\infty}\frac{1}{m^2}\int_0^{2\pi}\left(\frac{R_t}{R_t + a\cos\beta}\right)^m\right.$$
$$\left.\cdot\cos\beta\,\mathrm{d}\beta\cdot E_{m,M}(x,y)\right]. \tag{A13}$$

The position-dependent functions $E_{m,M}(x,y)$ are defined in Eq. (A19). The integral in Eq. (A13) can be solved by partial integration and the use of Ref. 40 (3.644-4),

$$A^{(2)} = \int_0^{2\pi}\ln(R_t + a\cos\beta)\cos\beta\,\mathrm{d}\beta = \int_0^{2\pi}\frac{b\sin^2\beta}{1+b\cos\beta}\mathrm{d}\beta$$
$$= \frac{2\pi}{b}\left(1-\sqrt{1-b^2}\right), \tag{A14}$$

with $b = a/R_t$.

The induced flux in segment M can be written as

$$\Phi_M(x,y) = -\mu_0 N_w I a\left[\frac{1-\sqrt{1-b^2}}{b}\,\frac{2\Delta\theta}{\pi} - \sum_{m=1}^{\infty}\frac{C_m(b)}{(m\pi)^2}\right.$$
$$\cdot\left(c_{m,M}\sum_{n=0}^{\lfloor\frac{m}{2}\rfloor}\binom{m}{2n}\left(\frac{x}{R_t}\right)^{m-2n}\left(\frac{y}{R_t}\right)^{2n}(-1)^n\right.$$
$$\left.\left.+ d_{m,M}\sum_{n=0}^{\lfloor\frac{m-1}{2}\rfloor}\binom{m}{2n+1}\left(\frac{x}{R_t}\right)^{m-(2n+1)}\left(\frac{y}{R_t}\right)^{2n+1}(-1)^n\right)\right]. \tag{A15}$$

The remaining integral in Eq. (A15),

$$C_m(b) = \int_0^{2\pi}\frac{\cos\beta}{(1+b\cos\beta)^m}\,\mathrm{d}\beta, \tag{A16}$$

is required for $m \geq 1$ and can be evaluated by recursion, as explained in Sec. I B.

With the substitutions,

$$D_0(b) = \frac{1-\sqrt{1-b^2}}{b}\,\frac{2\Delta\theta}{\pi},$$
$$D_m(b) = -\frac{C_m(b)}{(m\pi)^2} \quad \text{for} \quad m = 1,2,3,\ldots, \tag{A17}$$

the induced flux in quadrant M can be written as

$$\Phi_M(x,y) = -\mu_0 N_w I a\left[D_0(b) + \sum_{m=1}^{\infty} D_m(b)\,E_{m,M}(x,y)\right]. \tag{A18}$$

The position-dependent terms $E_{m,M}(x,y)$ are given by

$$E_{m,M}(x,y) = c_{m,M}\sum_{n=0}^{\lfloor \frac{m}{2} \rfloor}\binom{m}{2n}\left(\frac{x}{R_t}\right)^{m-2n}\left(\frac{y}{R_t}\right)^{2n}(-1)^n + d_{m,M}\sum_{n=0}^{\lfloor \frac{m-1}{2} \rfloor}\binom{m}{2n+1}\left(\frac{x}{R_t}\right)^{m-(2n+1)}\left(\frac{y}{R_t}\right)^{2n+1}(-1)^n. \tag{A19}$$

Analytic expressions for the functions $D_m(b)$ and the coefficients $c_{m,M}$ and $d_{m,M}$ are listed in Table III and for the functions $E_{m,M}(x,y)$ in Table IV up to order $m = 6$.

The symmetry relations for $E_{m,M}(x,y)$ in the different quadrants M, given in Table IV, apply to all orders in m and are passed on to the induced magnetic flux in a quadrant. Thus, given a magnetic flux in quadrant $M = 0$ of $\Phi_0(x,y)$, one finds for the induced fluxes in the other quadrants,

$$\begin{aligned}\Phi_1(x,y) &= \Phi_0(-x,y),\\ \Phi_2(x,y) &= \Phi_0(-x,-y),\\ \Phi_3(x,y) &= \Phi_0(x,-y).\end{aligned} \tag{A20}$$

The equivalence to Eq. (8) should be noted.

2. Recursion formula for $C_m(b)$

The difference of two consecutive functions is found to be proportional to the derivative of the first one,

$$\begin{aligned}C_{m+1}(b) - C_m(b) &= \int_0^{2\pi}\frac{\cos\beta}{(1+b\cos\beta)^m}\left(\frac{1}{1+b\cos\beta}-1\right)\mathrm{d}\beta\\ &= -b\int_0^{2\pi}\frac{\cos^2\beta}{(1+b\cos\beta)^{m+1}}\,\mathrm{d}\beta = \frac{b}{m}\frac{\mathrm{d}}{\mathrm{d}b}C_m(b).\end{aligned} \tag{A21}$$

Thus, the $(m+1)$th function can be obtained from the mth function by recursion via

$$C_{m+1}(b) = C_m(b) + \frac{b}{m}\frac{\mathrm{d}}{\mathrm{d}b}C_m(b), \tag{A22}$$

where following Eq. (A16), for $b \in (0,1)$, the function starting the recursion is found to be

$$C_1(b) = \int_0^{\pi}\frac{2\cos\beta}{1+b\cos\beta}\mathrm{d}\beta = \frac{2\pi}{b}\left(1-\frac{1}{\sqrt{1-b^2}}\right). \tag{A23}$$

3. Magnetic flux in one quadrant without displacement

Without displacements of the beam with respect to the center of the toroidal coil, i.e., for $x = y = 0$, the magnetic flux in Eq. (A18) is entirely given by the first term, yielding the well-known result,

$$\begin{aligned}\Phi_M(r=0) &= -\mu_0 N_w I a\, D_0(b)\\ &\approx -\mu_0 N_w I a\frac{b}{2}\\ &= -N_w\cdot\frac{\mu_0 I}{2\pi R_t}\cdot\pi a^2 = -N_w\cdot B\cdot S,\end{aligned} \tag{A24}$$

that the magnetic flux is equal to the product of the number of coil windings N_w, magnetic flux density B at a distance of R_t and the enclosed winding area S. (In the second line, we have made use of the fact that $b \ll 1$; see Table I.)

APPENDIX B: RESONANCE FREQUENCY OF QUARTER TOROID

The numerical calculation of the resonance frequency is carried out using the equivalent circuit diagram shown in Fig. 3. The relation of the measured output voltage U_M to the beam-induced voltage U_M^{ind} can be described in the frequency domain using the picture of a voltage divider, which leads to

$$\begin{aligned}\frac{U_M}{U_M^{\mathrm{ind}}} &= \frac{\left(\frac{1}{R_{\mathrm{out}}}+i\omega C\right)^{-1}}{i\omega L + R + \left(\frac{1}{R_{\mathrm{out}}}+i\omega C\right)^{-1}}\\ &= \frac{1}{(i\omega L+R)\left(\frac{1}{R_{\mathrm{out}}}+i\omega C\right)+1}.\end{aligned} \tag{B1}$$

The amplitude can be written as

$$F(\omega) = \left|\frac{U_M}{U_M^{\mathrm{ind}}}\right| = \frac{1}{\sqrt{\left(1-\omega^2 LC+\frac{R}{R_{\mathrm{out}}}\right)^2+\left(\frac{\omega L}{R_{\mathrm{out}}}+\omega RC\right)^2}}, \tag{B2}$$

and the phase is given by

$$\phi(\omega) = \arctan\left(\frac{\omega(CRR_{\mathrm{out}}+L)}{CLR_{\mathrm{out}}\omega^2 - R - R_{\mathrm{out}}}\right). \tag{B3}$$

To estimate C and L in this circuit, we consider the inner and outer radii of the toroidal coil,

$$\begin{aligned}r_i &= R_t - a = 52.5\,\mathrm{mm},\\ r_o &= R_t + a = 64.5\,\mathrm{mm},\end{aligned} \tag{B4}$$

using R_t and a, as listed in Table I.

The nominal outer wire diameter d_w is given by

$$d_w = 2r_w = 450\,\mu\mathrm{m}, \tag{B5}$$

and its insulation is 25 μm thick, i.e., the diameter of the current-carrying wire is 400 μm. The angle between two wire centers seen from the center of the toroid amounts to

$$\alpha = 2\arcsin\left(\frac{r_w}{r_i - r_w}\right). \tag{B6}$$

The maximum number of windings of a fully wound quadrant coil is, therefore, given by

$$N_w^{\mathrm{fq}} = \mathrm{floor}\left(\frac{\pi}{2\alpha}\right) = 182. \tag{B7}$$

In order to estimate the inductance of a quarter coil, we quote the textbook formula for a long, straight, and densely wound coil,

$$L^{\mathrm{fq}} = \mu_0\mu_r\frac{\left(N_w^{\mathrm{fq}}\right)^2}{\ell}S \approx 57.09\,\mu\mathrm{H}, \tag{B8}$$

TABLE IV. Analytical expressions for the terms $E_{m,M}(x,y)$ from Eq. (A19) for the four quadrants M up to order $m = 6$ for partial coverage of the quadrants.

M	0	1	2	3
	$E_{m,0}(x,y)$	$E_{m,1}(x,y)$	$E_{m,2}(x,y)$	$E_{m,3}(x,y)$
1	$\frac{x+y}{R_t}\,(\cos(\theta)-\sin(\theta))$	$E_{1,0}(-x,y)$	$E_{1,0}(-x,-y)$	$E_{1,0}(x,-y)$
2	$\frac{4xy}{R_t^2}\,\cos(2\theta)$	$E_{2,0}(-x,y)$	$E_{2,0}(-x,-y)$	$E_{2,0}(x,-y)$
3	$\frac{3\,x\,y^2-y^3-x^3+3\,x^2\,y}{R_t^3}\,(-\cos(3\theta)-\sin(3\theta))$	$E_{3,0}(-x,y)$	$E_{3,0}(-x,-y)$	$E_{3,0}(x,-y)$
4	$-2\,\frac{x^4-6x^2y^2+y^4}{R_t^4}\,\sin(4\theta)$	$E_{4,0}(-x,y)$	$E_{4,0}(-x,-y)$	$E_{4,0}(x,-y)$
5	$\frac{x^5+y^5+5\,x\,y^4+5\,x^4\,y-10\,x^2\,y^3-10\,x^3\,y^2}{R_t^5}\,(\cos(5\theta)-\sin(5\theta))$	$E_{5,0}(-x,y)$	$E_{5,0}(-x,-y)$	$E_{5,0}(x,-y)$
6	$\frac{12\,x\,y^5+12\,x^5\,y-40\,x^3\,y^3}{R_t^6}\,\cos(6\theta)$	$E_{6,0}(-x,y)$	$E_{6,0}(-x,-y)$	$E_{6,0}(x,-y)$

where N_w^{fq} is the number of windings of the quarter toroid, and $\ell = \frac{\pi}{2} r_i$ is the length of the coil along its inner radius. S denotes the cross section of the coil. Here, the permeability of vacuum is

$$\mu_0 = 1.256\,637\,061\,27(20)\cdot 10^{-6}\,\mathrm{V\,s\,A^{-1}\,m^{-1}}, \tag{B9}$$

and the relative permeability μ_r of the material of the coil body is close to unity.

As shown in Fig. 5, the coils do not cover the quadrants completely, and instead of N_w, given in Eq. (B7), the real number of windings used in a quarter coil amounted to

$$N_w = 132. \tag{B10}$$

The corresponding real inductance of a partially wound coil with the above-mentioned number of windings corresponds to

$$L = \frac{N_w}{N_w^{fq}}\cdot L^{fq} \approx 41.40\,\mu\mathrm{H}. \tag{B11}$$

The capacitances of the twisted connecting wires are estimated like in a parallel plate capacitor using a length and a plate separation of

$$\ell_C = 5\,\mathrm{cm} \quad \text{and} \quad d_C = 0.1\cdot d_w, \tag{B12}$$

yielding

$$C_{tw} = \epsilon_0 \cdot \frac{\ell_C \cdot d_w}{d_C} \approx 4.4\,\mathrm{pF}, \tag{B13}$$

where the vacuum permittivity is

$$\epsilon_0 \approx 8.854\times 10^{-12}\,\mathrm{A\,s\,V^{-1}\,m^{-1}}. \tag{B14}$$

These twisted wires are soldered to a 17 cm long coaxial cable with a specific capacity of 96 pF/m, resulting in a capacity of $C_{cc} = 16.3$ pF. This amounts to a total capacity,

$$C = C_{tw} + C_{cc} = 20.7\,\mathrm{pF}. \tag{B15}$$

An estimate of the resonance frequency of a quarter of a Rogowski coil using the specified geometrical and physical parameters given above, yields

$$f_0 = \frac{1}{2\pi\sqrt{LC}} \approx 5.44\,\mathrm{MHz}. \tag{B16}$$

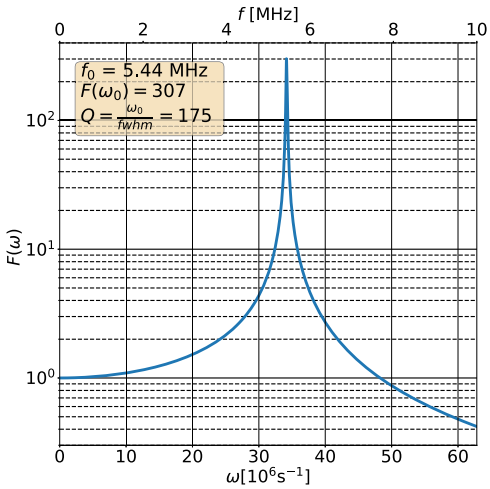

FIG. 18. Plot of the frequency response function $F(\omega)$ from Eq. (B2) using R_{out}, R, C, and L given in Table I. The resonance frequency f_0 is given in Eq. (B16), and the estimated quality factor $Q \approx 175$.

The resistance of a coil quarter amounts to

$$R = \frac{N_w \cdot 8(a+d_w)}{\sigma_{Cu}\cdot {d_w}^2} \approx 0.61\,\Omega, \tag{B17}$$

where for the conductivity of copper after winding, a value of

$$\sigma_{Cu} = 55\times 10^6\,\mathrm{S\,m^{-1}} \tag{B18}$$

was used.

The function $F(\omega)$ from Eq. (B2) is plotted in Fig. 18 using the values for C, L, R, and R_{out} listed in Table I. For an input impedance of $R_{out} = 500\,\mathrm{k}\Omega$, a quality factor for the operation of a quarter coil near the resonance ω_0 of

$$Q = \frac{\omega_0}{\mathrm{fwhm}} \approx 175 \tag{B19}$$

can be estimated.

APPENDIX C: EFFECT OF MIRROR CURRENTS

The distribution of the image current density for a pencil beam depends on its position (r, ψ),[12]

$$j(\rho,\phi) = \frac{-I}{2\pi\rho}\,\frac{\left(1-\alpha^2\right)\delta(\rho-u)}{1-2\alpha\,\cos\left(\phi-\psi\right)+\alpha^2} = \frac{-I}{2\pi\rho}\left[1+2\sum_{m=1}^{\infty}\alpha^m\,\cos\left(m(\phi-\psi)\right)\right]\delta(\rho-u), \tag{C1}$$

with

$$\alpha = \frac{r}{\rho},$$

where the delta-function has been introduced to state that the current density is confined to the inner tube surface because of the skin effect. The inner radius of the beam tube is denoted by u, and the beam coordinates r and ψ are defined in Eq. (A7). On integrating, one finds that the total current on the wall matches exactly the beam current I.

A pickup coil, such as a segmented Rogowski coil, not only captures the magnetic field of the beam but also that of the wall currents, which constructively adds to the primary contribution by the beam because these currents flow on the other side of the coils in the reverse direction. The total flux through a coil due to the wall currents can be found similar to the discussion of Eq. (A1). Equation (5) is a special case of the more general expression of the vector potential for a two-dimensional current distribution,

$$A_z(\rho,\phi) = \frac{\mu_0}{2\pi}\int_{R^2} j(\vec{r}\,')\ln\left(|\vec{r}(\rho,\phi)-\vec{r}\,'|\right)\mathrm{d}\vec{r}\,', \tag{C2}$$

which, for the wall currents, takes the following form:

$$A_z(\rho,\phi) = \frac{\mu_0 I}{4\pi^2}\int_0^{2\pi}\int_0^{\infty}\frac{1}{\rho'}\,\frac{\left(1-\alpha'^2\right)\delta(\rho'-s)}{1-2\alpha'^2\,\cos\left(\phi'-\psi\right)+\alpha'^2} \cdot \ln\left(\sqrt{\rho'^2-2\rho'\rho\,\cos\left(\phi'-\phi\right)+\rho^2}\right)\rho'\mathrm{d}\rho'\mathrm{d}\phi' \tag{C3}$$

with

$$\alpha' = \frac{r}{\rho'}.$$

In order to find the lowest-order term $(m = 1)$ in the displacement, we can expand both the fraction and the logarithm [see Eq. (A8)],

$$A_z(\rho,\phi) = \frac{\mu_0 I}{8\pi^2}\int_0^{2\pi}\left(1+2\frac{r}{u}\cos\left(\phi'-\psi\right)\right) \cdot\left(\ln\left(u\right)-\frac{\rho}{u}\cos\left(\phi'-\phi\right)\right)\mathrm{d}\phi' \tag{C4}$$

and see that only the product of the two cos terms yields the desired contribution,

$$A_z(\rho,\phi) = -\frac{\mu_0 I}{4\pi^2}\frac{r\rho}{u^2}\int_0^{2\pi}\cos\left(\phi'-\psi\right)\cos\left(\phi'-\phi\right)\mathrm{d}\phi' = -\frac{\mu_0 I}{4\pi}\frac{r\rho}{u^2}\cos\left(\phi-\psi\right). \tag{C5}$$

Analogous to Eq. (A5), the flux induced in the quadrant coil M is obtained by the integration over its surface,

$$\Phi_M = \frac{2aN_w}{\pi}\int_{M(\pi/2)-\theta}^{(M+1)(\pi/2)+\theta}\int_0^{2\pi}A_z(\rho(\beta),\beta)\cos\left(\beta\right)\mathrm{d}\beta\mathrm{d}\phi = \frac{a\mu_0 N_w I}{2\pi^2}\frac{r}{u^2}\int_0^{2\pi}\left[R_t+a\,\cos\left(\beta\right)\right]\cos\left(\beta\right)\mathrm{d}\beta \cdot\int_{M(\pi/2)+\theta}^{(M+1)(\pi/2)-\theta}\cos\left(\phi-\psi\right)\mathrm{d}\phi, \tag{C6}$$

$$\Phi_M(x,y) = \frac{a\mu_0 N_w I}{2\pi^2}\frac{r}{u^2}a\pi\left[c_{1,M}\,\cos\left(\psi\right)+d_{1,M}\,\sin\left(\psi\right)\right] = \frac{\mu_0 N_w I}{2\pi}\frac{a^2}{u^2}\left[c_{1,M}\,x+d_{1,M}\,y\right], \tag{C7}$$

with the coefficients $c_{1,M}$ and $d_{1,M}$ defined in Eq. (A10). In particular,

$$\Phi_0(x,y) = \frac{\mu_0 N_w I}{2\pi}\frac{a^2}{u^2}(\cos\,\theta-\sin\,\theta)(x+y) = \mu_0 N_w I a\left(\frac{aR_t}{2\pi u^2}\right)E_{1,0}(x,y). \tag{C8}$$

This flux adds to the primary one from the beam current; see Eq. (A18). There, the term in brackets has its beam current counterpart in

$$D_1(b) = \frac{2}{b\pi}\left(\frac{1}{\sqrt{1-b^2}}-1\right)\approx\frac{b}{\pi}, \tag{C9}$$

which is about half the value in brackets for a Rogowski quarter coil close to the beam tube $u \approx R_t$. This explains, in part, the about 50% higher value of the linear term of the induced voltage with respect to the displacement found experimentally; see the discussion following Eq. (17).

REFERENCES

[1] M. Pospelov and A. Ritz, Ann. Phys. **318**, 119 (2005) special Issue.
[2] B. Robson, J. High Energy Phys., Gravitation Cosmol. **4**, 166 (2018).
[3] W. Bernreuther, "Cp violation and baryogenesis," in *CP Violation in Particle, Nuclear and Astrophysics*, edited by M. Beyer (Springer, Berlin, Heidelberg, 2002), pp. 237–293.
[4] F. Abusaif, A. Aggarwal, A. Aksentev, B. Alberdi-Esuain, A. Andres, A. Atanasov, L. Barion, S. Basile, M. Berz, M. Beyß *et al.*, *CERN Yellow Report No. CERN-2021-003* (CERN, 2021), p. 257.
[5] F. Rathmann, A. Saleev, and N. N. Nikolaev, JEDI, and srEDM, J. Phys. Conf. Ser. **447**, 012011 (2013).
[6] W. M. Morse, Y. F. Orlov, and Y. K. Semertzidis, Phys. Rev. Spec. Top. Accel. Beams **16**, 114001 (2013).
[7] F. Rathmann, N. N. Nikolaev, and J. Slim, Phys. Rev. Accel. Beams **23**, 024601 (2020).
[8] R. Maier, Nucl. Instrum. Methods Phys. Res., Sect. A **390**, 1 (1997).
[9] C. Weidemann *et al.*, Phys. Rev. Spec. Top. Accel. Beams **18**, 020101 (2015).
[10] T. Wagner, A. Nass, J. Pretz, F. Abusaif, A. Aggarwal, A. Andres, I. Bekman, N. Canale, I. Ciepal, G. Ciullo *et al.*, J. Instrum. **16**, T02001 (2021).
[11] J. Slim, R. Gebel, D. Heberling, F. Hinder, D. Hölscher, A. Lehrach, B. Lorentz, S. Mey, A. Nass, F. Rathmann *et al.*, Nucl. Instrum. Methods Phys. Res., Sect. A **828**, 116 (2016).
[12] M. Wendt, IEEE Instrum. Meas. Mag. **24**, 21 (2021).

[13]R. E. Shafer, AIP Conf. Proc. **249**, 601 (1992).
[14]H. Koziol, *CAS - CERN Accelerator School: Basic Course on General Accelerator Physics* (CERN, 2005).
[15]J. Harasimowicz, C. P. Welsch, L. Cosentino, A. Pappalardo, and P. Finocchiaro, Phys. Rev. Spec. Top. Accel. Beams **15**, 122801 (2012).
[16]J. García Garrigós, "Development of the beam position monitors for the diagnostics of the test beam line in the CTF3 at CERN," Ph.D. thesis, Universitat Politècnica de València, 2013.
[17]J. Cupérus, Nucl. Instrum. Methods **145**, 219 (1977).
[18]M. Gasior, in 6th European Workshop on Beam Diagnostics and Instrumentation for Particle Accelerators, 2003.
[19]T. Kobayashi, T. Kozawa, T. Ueda, M. Uesaka, K. Miya, and H. Shibata, Nucl. Instrum. Methods Phys. Res., Sect. A **361**, 436 (1995).
[20]S. Battisti, M. Le Gras, J. M. Roux, B. Szeless, and D. J. Williams, Report No. CERN-PS-BR-87-37, 1987.
[21]N. Baboi, A. Brenger, D. Lipka, J. Lund-Nielsen, and K. Wittenburg, "DESY," in *14th Beam Instrumentation Workshop, Santa Fe, New Mexico, USA* (JACoW, Geneva, 2010), pp. 214–217.
[22]F. Hinder, H.-J. Krause, H. Soltner, and F. Trinkel, in 4th International Beam Instrumentation Conference, 2016.
[23]F. Abusaif, "Development of compact, highly sensitive beam position monitors for storage rings," Ph.D. thesis, RWTH Aachen University, 2021.
[24]D. Berners and L. Reginato, AIP Conf. Proc. **281**, 168 (1992).
[25]P. Forck, D. Liakin, and P. Kowina, *CERN Accelerator School, Beam Diagnostics* (CERN, 2008), pp. 187–228.
[26]S. Haciömeroglu, D. Kawall, Y.-H. Lee, A. Matlashov, Z. Omarov, and Y. K. Semertzidis, in *Proceeding of Science International Conference of High Energy Physics 2018* (Proceedings of Science, 2019), p. 279.
[27]W. Rogowski and W. Steinhaus, Arch. Elektrotech. **1**, 141 (1912).
[28]V. Nassisi and A. Luches, Rev. Sci. Instrum. **50**, 900 (1979).
[29]D. G. Pellinen, M. S. Di Capua, S. E. Sampayan, H. Gerbracht, and M. Wang, Rev. Sci. Instrum. **51**, 1535 (1980).
[30]R.-Y. Han, W.-D. Ding, J.-W. Wu, H.-B. Zhou, Y. Jing, Q.-J. Liu, Y.-C. Chao, and A.-C. Qiu, Rev. Sci. Instrum. **86**, 035114 (2015).
[31]M. H. Samimi, A. Mahari, M. A. Farahnakian, and H. Mohseni, IEEE Sens. J. **15**, 651 (2015).
[32]D. A. Ward and J. L. T. Exon, Eng. Sci. Educ. J. **2**, 105 (1993).
[33]S. S. Kurennoy, Phys. Rev. ST Accel. Beams **4**, 092801 (2001).
[34]R. W. Helms and G. H. Hoffstätter, in 9th European Particle Accelerator Conference, 2004.
[35]G. Grandi, M. Kazimierczuk, A. Massarini, and U. Reggiani, IEEE Trans. Ind. Appl. **35**, 1162 (1999).
[36]S. Merzliakov, C. Böhme, and V. Kamerdzhiev, *IKP Annual Report* (Forschungszentrum Jülich, 2016).
[37]C. Böhme, I. Bekman, V. Kamerdzhiev, B. Lorentz, M. Simon, and C. Weidemann, in 6th International Beam Instrumentation Conference, 2018.
[38]F. Terman, *Radio Engineer's Handbook*, *McGraw-Hill handbooks* (McGraw-Hill Book Company, Incorporated, 1943).
[39]J. D. Jackson, *Classical Electrodynamics* (Wiley, 1975).
[40]I. S. Gradstein and Ryshik, *Table of Integrals, Series, and Products* (Harry Deutsch, 1981).